

Effect of Oxygen Vacancy Concentration on the Photocatalytic Hydrogen Evolution Performance of Anatase TiO₂: DFT and Experimental Studies

Shufang Jia

Taiyuan University of Technology School of Materials Science and Engineering

Jiaqi Gao

Taiyuan University of Technology School of Materials Science and Engineering

Qianqian Shen

Key Laboratory of Science and Engineering in Advanced Materials (Taiyuan University of Technology)

Jinbo Xue

Key Laboratory of Interface Science and Engineering in Advanced Materials (Taiyuan University of Technology)

Zhuxia Zhang

Key Laboratory of Interface Science and Engineering in Advanced Materials (Taiyuan University of Technology)

Xuguang Liu

Taiyuan University of Technology School of Materials Science and Engineering

Husheng Jia (✉ jia_husheng@126.com)

Taiyuan University of Technology School of Materials Science and Engineering <https://orcid.org/0000-0001-8257-8874>

Research Article

Keywords: Oxygen vacancy, First-principles calculation, Anatase TiO₂ (101), Catalytic activity

Posted Date: March 12th, 2021

DOI: <https://doi.org/10.21203/rs.3.rs-282876/v1>

License:   This work is licensed under a Creative Commons Attribution 4.0 International License.

[Read Full License](#)

Version of Record: A version of this preprint was published at Journal of Materials Science: Materials in Electronics on April 18th, 2021. See the published version at <https://doi.org/10.1007/s10854-021-05915-5>.

Abstract

Oxygen vacancies (OVs) are important for changing the geometric and electronic structure as well as the chemical properties of anatase TiO_2 . In this work, we performed a DFT calculation on the electronic structure and catalytic performance of anatase TiO_2 (101) with different numbers of OVs. A comparison of the measured XRD results with the simulated ones of TiO_2 demonstrates that OVs can cause changes in the crystal structure. The changes in the electronic structure (Mulliken charges, band structure, and partial density of states) and water splitting on TiO_2 (101) surfaces were investigated as a function of oxygen vacancy concentration. The results show that the introduction of oxygen vacancy forms impurity levels below the conduction band of Ti 3d orbitals, and electrons can gradually transit from VB to CB through the impurity levels. However, when oxygen vacancy concentration is too high, the maximum electron transition energy increases and the promotion effect of oxygen vacancy on water splitting is weakened. This work would provide more enlightenment and information for the design of defective TiO_2 with higher photocatalytic activity.

1 Introduction

The increasing consumption of fossil energy has caused serious energy crisis and environmental problems. Hydrogen as a renewable and environmentally friendly new energy has attracted great attention of scientific community [1]. In 1972, Fujishima and Honda found hydrogen production from H_2O splitting on a TiO_2 photoelectrode [2], inspiring much concern on semiconductor photocatalytic materials from scientists in the scientific field. Solar energy is a kind of renewable green energy, and its use for semiconductor-based photocatalytic water splitting to produce hydrogen has been considered as one of the most important solutions to world energy crisis [3]. Titanium dioxide (TiO_2) is perhaps one of the most important materials used as photocatalyst for hydrogen generation owing to its excellent properties such as superior photostability, non-toxicity, abundant reserves, and low cost [4–6]. Two common crystal types of TiO_2 are anatase and rutile, which have high catalytic activity and stability. However, TiO_2 is a wide band gap semiconductor (rutile: 3.0 eV; anatase: 3.2 eV), and only absorbs ultraviolet light that accounts only for about 5% of the solar energy. Therefore, its solar energy utilization efficiency is very low, making it impossible for large-scale industrial applications [7, 8]. Hence, improving the optical sensitivity and activity of TiO_2 in the visible light region has been explored with strategies based on doping, ion implantation, metal loading, and composite semiconductors [9, 10]. In recent years, self-doped oxygen vacancy has been extensively studied experimentally and theoretically. This doping method features not only low cost, but also the ease in preparation and high effectiveness [11, 12].

The research results have shown that oxygen vacancies in TiO_2 are preferential active sites for molecular adsorption and dissociation, in addition to being traps for photoexcited charged carriers [13,14]. Zuo et al. [15] reported a one-step method to synthesize Ti^{3+} -doped TiO_2 . Both theoretical calculations and experimental results confirmed that the introduction of Ti^{3+} extends the photocatalytic activity from ultraviolet to visible light. In our previous work, black TiO_2 nanotubes with oxygen vacancies (OVs) were

prepared, and through experimental characterizations, the enhancement in photocatalytic performance by the introduction of OV was proved [16]. The excess electrons and Ti^{3+} sites generated by OVs affect the adsorption and reaction of adsorbate on TiO_2 surface, and significantly improve its photocatalytic performance [17]. Hinuma et al. [18] used density functional theory (DFT) to calculate E_{Ovac} on various semiconductor oxide surfaces at the same computational level, and investigated the adsorption of small molecules on anoxic surfaces. The results showed that their adsorption energy and adsorption mode are strongly dependent on E_{Ovac} . Moreover, Kong et al. [19] reported that the concentration of bulk OVs in TiO_2 can adjust the photocatalytic efficiency. Wei et al. [20] investigated the adsorption properties of H_2S on rutile TiO_2 (110) surface with different OV coverage. Since oxygen vacancy has an important effect on photocatalytic activity, it is of great significance to introduce oxygen vacancy in a controlled manner.

In the past, a large number of experiments and theoretical calculations have mainly focused on the properties of rutile TiO_2 (110), including those from the introduction of OVs and for the interaction with water [21–23]. Recently, some studies have shown that anatase has a higher photocatalytic activity than rutile, so the most stable (101) surface in anatase has recently received a lot of attention [24–26]. Therefore, in this work, we investigated the surface properties of anatase TiO_2 (101) surface at different OV concentration (0/8, 1/8, 2/8, 3/8 monolayer) and their effect on the surface adsorption and dissociation of water.

In present study we combined the experimental and theoretical aspects to investigate the influence of OV concentration on the electronic structure and catalytic performance of anatase TiO_2 (101). First, the XRD patterns of TiO_2 crystals with different OV concentrations were simulated and compared with the experimental XRD patterns of TiO_2 samples to explore the relationship between crystalline phase and OV_{S} . Second, a stable TiO_2 (101) surface was selected to examine the effect of OV concentrations on anatase (101) geometry and electronic structure. Finally, by calculating the dissociation transition state of H_2O on the surface of TiO_2 (101), the influence of OV concentration on water dissociation was analyzed. The results of DFT calculation show that moderate OV concentration can improve the transition ability of electrons. This work is expected to have a theoretical guidance for the use of anatase TiO_2 (101) surface as a catalyst for the photolysis of water to produce hydrogen.

2 Experimental And Computational Details

2.1 Experimental Details

TiO_2 nanotube arrays were prepared by electrochemical anodic oxidation. Titanium sheets were ultrasonically cleaned with acetone, ethanol, and deionized water, and then anodized in 100 mL of NH_4F ethylene glycol (EG) solution (0.47 g of NH_4F , 98 mL of EG, and 2 mL of deionized water) at 50 V for 1 h at room temperature with a platinum plate as counter electrode. The as-anodized samples were thoroughly cleaned with deionized water, wrapped with aluminum powder and annealed at 300°C, 450°C

and 600°C separately in argon for 2 h with a heating rate of 2°C/min, denoted as B-TiO₂-300, B-TiO₂-450, and B-TiO₂-600, respectively. For comparison, TiO₂ nanotube arrays were annealed in air at 450°C for 2 h to give a control sample without oxygen vacancies, which is denoted as TiO₂-Air. The phase structure of samples was characterized by employing X-ray diffraction (XRD) with Cu K α irradiation ($\lambda = 1.5406 \text{ \AA}$) operating at 40 kV tube voltage and 30 mA tube current. The diffraction patterns between 20° and 80° (2 θ) were collected in a step of 0.02°. JEOL JES-FA200 EPR spectrometer was used to record electron paramagnetic resonance (EPR) spectra at room temperature. UV-vis diffused reflectance spectroscopy (DRS) results were collected on a PerkinElmer Lambda 950 spectrophotometer in wavelength range of 300–800 nm.

Hydrogen evolution tests of two pieces of black TiO₂ nanotube arrays were carried out in a 100 mL photochemical quartz cell containing 100 mL of deionized water, and 20 mL of methanol as the sacrificial reagent. Then, 66 μL of H₂PtCl₆ (15 mg/mL) was injected into the mixed solution. The suspensions were maintained strictly at 3°C by re-circulating cooling water system. The system was deaerated by bubbling N₂ into the solution for 20 min before light irradiation. The excitation light source was a 300 W Xenon lamp equipped with a UV-cutoff filter (> 420 nm), and the light intensity was measured to be 100 mW/cm². The reaction system was irradiated for about 5 hours, and H₂ amount was measured by an 8890 Gas Chromatograph System equipped with a thermal conductivity detector (TCD).

2.2 Computational Method and Models

All the calculations in this work were completed by using the Cambridge Serial Total Energy Package (CASTEP) module of Materials Studio (MS). The plane-wave ultrasoft pseudopotential based on density functional theory (DFT) was adopted, and the exchange-related energy was calculated by the PBE functional under Generalized Gradient Approximation (GGA) [27]. Because conventional DFT calculations based on the local density approximation cannot truly describe the electronic correlation in transition metal oxides, DFT + U method was introduced to evaluate the on-site coulombic interactions in the localized d orbital and exchange interactions, by adding an effective Hubbard-U parameter to express the repulsion between electrons on the same orbital [28]. In our calculations, the value of U parameter was determined to be 3.5 eV for Ti atom [29, 30]. The valence electron configurations are 3d²4s² for Ti and 2s²2p⁴ for O, respectively. The energy cutoff for the plane wave basis set was selected as 380 eV, and a 3 \times 3 \times 1 Monkhorst–Pack k-point grid was used to integrate the Brillouin zone. The convergence criteria of energy, maximum force, maximum stress, and maximum displacement are 1 \times 10⁻⁵ eV/atom, 0.03 eV/ \AA , 0.05 GPa, and 0.001 \AA , respectively. The optimized anatase TiO₂ lattice parameters are a = b = 3.79 \AA and c = 9.77 \AA , which are consistent with the previous experimental and theoretical results [31–33].

Table 1 Formation energy of OV_s at different positions

Model	OVs site	$E_{\text{Ovf}} / \text{eV}$
1/8ML	1	4.69
2/8ML	1-2	4.93
	1-6	4.88
	1-7	4.86
3/8ML	1-2-7	5.04
	1-4-7	5.02

In this work, a (1 × 4) anatase (101) surface supercell was used as the slab model with three O–Ti–O layers, and the underlying O–Ti–O layer was fixed to simulate the bulk atomic structure, as shown in Fig. 1. In order to avoid the interaction between adjacent surfaces, a 20 Å vacuum layer was installed for all systems. This structural model has proved to be very reliable in many studies [34, 35]. On the basis of this model, the anatase TiO₂ (101) surface models with different concentration of OVs (0/8, 1/8, 2/8, 3/8 ML) were constructed by removing the two-fold coordinated O atom (one, two, three), and the removed O atoms denoted as OVs are marked with black circles, as shown in Fig. 2a–c. By calculating the formation energy of oxygen vacancy at different positions, as shown in Table 1, the models with less vacancy formation energy were selected for calculation, as shown in Fig. 2. The OV formation energy (E_{Ovf}) at each position was calculated by the following formula:

$$E_{\text{Ovf}} = E_{\text{tot(defect)}} - E_{\text{tot(perfect)}} + n_0 \mu_0 \quad (1)$$

where, $E_{\text{tot(perfect)}}$ and $E_{\text{tot(defect)}}$ are the total energy of perfect anatase TiO₂ (101) surface and anatase TiO₂ (101) surface with oxygen vacancies, respectively, μ_0 the chemical potential of oxygen atom, and n_0 the number of oxygen atoms removed from the perfect supercell. Adsorption energies were obtained by

$$E_{\text{ads}} = E_{\text{surf-H}_2\text{O}} - (E_{\text{surf}} + E_{\text{H}_2\text{O}}) \quad (2)$$

where, $E_{\text{surf-H}_2\text{O}}$, E_{surf} , and $E_{\text{H}_2\text{O}}$ are the total energies calculated for the slab with adsorbate, the clean stoichiometric slab, and the adsorbate in gas phase, respectively.

Since it is difficult to evaluate the solvent effect of a real liquid reaction in the solid surface system, during the adsorption and dissociation of water molecule, we only consider the adsorption and decomposition behavior of water molecules on the surface of defective anatase TiO₂ (101) in the case of no solvent (i.e. in the gas environment). The most stable adsorption and dissociation configurations of water molecules on the surface were optimized, and these two configurations were set as the initial state (reactant) and final state (product), respectively. Complete linear synchronous transit (LST) and quadratic synchronous transit (QST) approaches were chosen to search for transition states, and then the nudged elastic band (NEB) method was used to determine the transition state on the minimum reaction energy

path [36–38]. According to the calculated adsorption energy of these states, the reaction activity and energy of water splitting reaction on the surface of anatase TiO_2 (101) with different oxygen vacancy concentration were analyzed.

3 Results And Discussion

3.1 Structural characteristics of anatase TiO_2 catalysts

Black TiO_2 nanotube arrays were prepared by anodic oxidation and aluminum powder reduction. The crystallinity and phase composition of black TiO_2 nanotube arrays after annealing at different temperatures were characterized by X-ray diffraction (XRD), and the XRD patterns of the prepared TiO_2 nanotube arrays are shown in Fig. 3a. Black TiO_2 nanotube arrays have a high degree of crystallinity and characteristic diffraction peaks similar to anatase TiO_2 , corresponding to the reflective crystal planes of (101), (004), (105), (204), (116), (220), and (301). In the measured XRD patterns in Fig. 3a, a new diffraction peak appears at 2θ 33.8° , and the higher the annealing temperature, the higher the intensity of the peak. The reason may be that a large amount of charge generated by the oxygen vacancies causes the charge in the valence of cation, so that anatase TiO_2 is reduced to form a new stable phase [40]. In order to further prove that the changes in the surface structure of black TiO_2 nanotube arrays are caused by oxygen vacancies, electron paramagnetic resonance (EPR) was used to detect the presence of oxygen vacancies. The g factor of the signal is equal to 1.994, which corresponds to the surface oxygen vacancies, as shown in Fig. 3b [41, 42]. With the increase of aluminothermic reduction temperature, the intensity of the EPR signal becomes stronger, suggesting the increase of oxygen vacancy concentration on the surface of black TiO_2 nanotube arrays. This finding is consistent with the conclusion obtained from XRD results.

For materials with known structures, it is a commonly used method to calculate theoretical XRD patterns by software[43]. In this section, XRD patterns were simulated by the Reflex software package from Materials Studio (MS) according to the crystal structure. Therefore, a 48-atom $2 \times 2 \times 1$ supercell ($\text{Ti}_{16}\text{O}_{32}$) was used to simulate the XRD patterns of anatase TiO_2 with different numbers of OVs, and compare them with the experimental XRD patterns of TiO_2 samples. As shown in Fig. 3c, a $\text{Ti}_{16}\text{O}_{32}$ model with 2, 4, or 6 OVs was constructed to form OV concentration of 1/16, 1/8, and 3/16, respectively. As shown in Fig. 3d, in the simulated XRD patterns of anatase TiO_2 crystals containing different numbers of OVs, a new diffraction peak also appears at 33.8° . As the OV concentration increases, the peak intensity at 33.8° increases proportionally. These results indicate that there are different numbers of OVs in black TiO_2 nanotube arrays, as also shown in the XRD patterns in Fig. 3a. Therefore, the anatase TiO_2 crystal (Fig. 3c) can represent the structure of TiO_2 obtained at different aluminothermic temperatures. Consequently, computational simulation was adopted to explore the properties of anatase TiO_2 with different OV concentration, and evaluate the difference in its electronic structure from a theoretical perspective.

3.2 Influences of OV_S on the geometrical and electronic structure and optical properties of anatase TiO_2 (101)

3.2.1 Geometry structure

The introduction of oxygen vacancy on the surface of TiO_2 (101) causes lattice distortion of its surface structure. The original Ti_{6c} and Ti_{5c} atoms bonded to the O_{2c} atoms at the vacancies become 5- and 4-coordinated, denoted as Ti_{v-5c} and Ti_{v-4c} , respectively. On the optimized defect surface, the removal of O atoms from the surface of lattice strengthens the relationship between adjacent Ti atoms and other adjacent O atoms, and shortens the length of Ti–O bonds. The calculated results are consistent with the experimental ones [42].

By comparing the optimized surface structures, we conducted a detailed analysis on the same position of the surface, as shown in Fig. 4, and found that different concentration of oxygen vacancy causes different degree of lattice distortion of the surface structure. The O_{3c} on the surface of 1/8 ML oxygen vacancy relaxes upwards by 0.23 Å, and Ti_{v-5c} and Ti_{v-4c} relax inwardly by 0.32 and 0.28 Å, respectively, which results in the change in $Ti_{v-5c}-O-Ti_{v-4c}$ on the surface structure from 94.16° to 130.21°. The O_{3c} on the surface of 2/8 ML oxygen vacancies relaxes upwards by 0.29 Å, and Ti_{v-5c} and Ti_{v-4c} relax inwardly by 0.32 and 0.26 Å, respectively, which results in the enlargement of $Ti_{v-5c}-O-Ti_{v-4c}$ on the surface structure from 94.16° to 134.56°. The O_{3c} on the surface of the 3/8 ML oxygen vacancies relaxes upwards by 0.27 Å, and Ti_{v-5c} and Ti_{v-4c} relax inwardly by 0.34 and 0.22 Å, respectively, which results in the increase in $Ti_{v-5c}-O-Ti_{v-4c}$ on the surface structure from 94.16° to 133.28°. Through the research on the adsorption of H_2O on the surface in the following section, it is found that the increase in lattice distortion can enhance the adsorption of H_2O on the surfaces.

3.2.2 Electronic structure

In order to understand the effects of OV concentration on the electronic structure of anatase TiO_2 (101) surface, the Mulliken charge, differential charge density, band structure, and partial density of states (PDOS) as a function of OV concentration were calculated. Table 2 shows the average Mulliken charges of Ti atoms on the surface structure of anatase TiO_2 (101). It can be found that the Mulliken charges of Ti atoms decrease with the increase of oxygen vacancy concentration, which is due to the redistribution of excess electrons generated by oxygen vacancy in the position of adjacent Ti atoms. The effect of average Mulliken charge on anatase TiO_2 (101) is also shown in the differential charge density diagram of anatase TiO_2 (101) with OVs. As shown in Fig. 5, the charge density of Ti atoms on the surface around OVs is increased significantly. It is worth noting that when the number of OVs increases to 3, the charge density of Ti atoms next to the OVs is relatively weakened.

Table 2
Average Mulliken charge of TiO₂ (101) with OV_s

Model	Total Ti atoms	Surface Ti atoms
0/8 ML	1.395	1.390
1/8 ML	1.328	1.316
2/8 ML	1.317	1.296
3/8 ML	1.307	1.273

In order to further analyze the influence of OV concentration on the electronic structure of anatase TiO₂ (101), the band structures and density of states of the four different models (0/8, 1/8, 2/8, 3/8 ML) were calculated on the basis of structural optimization. The comparison of our results with the previous research results of the electronic properties of the defect anatase (101) surface is summarized in Table 3.

Table 3
Band gaps (E_g) of defect anatase (101) surface under varying computational parameters

Anatase (101)	E_g (eV)	Method	Reference
O _v -surf	2.78	DFT+(U = 3.5)	This work
O _v -surf	2.32	DFT+(U = 3.0)	[15]
O _v -surf	2.10	DFT+(U = 3.0)	[28]
O _v -surf	1.58	DFT + D	[28]
O _v -surf	2.59	DFT+(U = 3.0)	[44]
O _v -surf	2.80	DFT+(U = 4.0)	[44]
O _v -surf	3.15	HSE06	[45]

As shown in Fig. 6, compared with the perfect surface, the surface with OV exhibits a defective state at 0.8–1.0 eV below the conduction band, which is consistent with the previously reported results [12, 46]. The removal of neutral oxygen atoms to form OV can lead to the redistribution of excess electrons between adjacent Ti atoms near the OV site, thus to the formation of shallow donor impurity levels below the conduction band of Ti 3d orbitals, and the number of impurity levels increase with the increase of OV [47]. As a result, anatase TiO₂ (101) shows the characteristics of n-type semiconductor. In this case, the band gap increases by 0.1–0.3 eV, which is consistent with bulk TiO₂ [48–50]. The existence of the defect state is equivalent to building a step between VB and CB, so that electrons can gradually transit from VB to CB. For anatase TiO₂ (101) surfaces with monolayer OV concentration of 1/8, 2/8, and 3/8 ML, the

maximum transition energy between different energy levels is 1.888, 1.888, and 1.901 eV, respectively. Electron transitions on defect surfaces are easier than on perfect surface. By comparing the surfaces with different OV concentration, it is found that the maximum transition energy of the surfaces with three oxygen vacancies is the greatest. As mentioned earlier, this is caused by the relative weakening of the charge density of Ti atoms next to the OVs. This shows that moderate OV concentration can improve the electron transition ability, but an excessively high OV concentration may lead to the weakening of this enhancement effect.

The PDOS of anatase TiO₂ (101) surface with different OV concentration is shown in Fig. 7. Pure anatase TiO₂ (101) conduction band is mainly composed of Ti 3d orbitals, while the valence band is mainly composed of O 2p orbitals, and the Fermi level is close to the top of the valence band. By comparing the density of states between a perfect surface and a surface with OVs, it is clear that the OV makes the Fermi level move into the bottom of the conduction band, and the surface structure presents the characteristics of n-type semiconductor. After the introduction of oxygen vacancy onto the surface, the total density of states of the system shifts to a lower energy level. Moreover, as the OV concentration increases, the total density of states shifts to an even lower energy level, and the Fermi energy level moves further into the conduction band. From the band gap, it can be found that the defect state is caused by OVs, and mainly contributed on Ti 3d. Most of the excess electrons are localized on Ti atoms, consistent with the results obtained from Table 2 analysis.

3.2.3 Optical properties

As can be seen from Fig. 8a, the light absorption curves of the anatase TiO₂ (101) surface system with OVs exhibit blue shift to a certain extent, which is mainly due to the existence of OVs and the widening of the band gap of the system. The introduction of OVs improves the light absorption performance of anatase TiO₂ (101), which is mainly reflected in the obvious increase in the visible light (500–780 nm) range, and in the significant increase in the relative light absorption coefficient. The electron at the top of valence band is first excited to the impurity level, and then absorbs a photon with smaller energy to achieve indirect transition. More information can be obtained by analyzing the dielectric function. It can be seen from Fig. 8b that an obvious peak of dielectric function appears for the defect surface in the range of 0–2.80 eV, but it does not appear for perfect anatase TiO₂ (101), indicating that the peak is induced by OV on the surface. In the range of 2.80–4.80 eV, the dielectric peaks of the defect surface and perfect surface are roughly the same in shape, but slightly different in peak strength, indicating that the existence of OV has great influence on the energy band structure near the band gap. It can be also seen from Fig. 8b that the imaginary part ϵ_2 of the dielectric function of defect anatase TiO₂ (101) surface shifts to higher energy to varying degree. Its light wave absorption threshold produces a blue shift, which is consistent with the results obtained from the light absorption spectra.

The light absorption properties of the samples at different annealing temperatures and the corresponding band gap plots were obtained experimentally study, as shown in Fig. 9. Compared with TiO₂-Air, black

TiO₂ nanotube arrays show stronger absorption in the visible region, as shown in Fig. 9a, which is consistent with the calculation results. It can be seen from the indirect interband transition energies that when the temperature reaches 600 °C, the band gap increases from 2.81 to 2.90 eV. This finding indicates that when the OV concentration is too high, the enhancement effect of OV on the performance of TiO₂ is weakened, which is in line with the conclusion of the previous band discussion.

3.3 H₂O adsorption and decomposition on anatase TiO₂ (101) surface with OV_S

In order to examine the adsorption and dissociation process of H₂O on the surface of TiO₂ (101) with different OV concentrations, the same number of H₂O molecules are adsorbed on different surfaces to analyze the effect of OV concentration on hydrolysis by calculating the dissociation transition state. Previous studies [15, 18, 51, 52] found that the most stable adsorption configuration for water on the surface of pure anatase TiO₂ (101) is to bond with the Ti_{5c} atom and form weak hydrogen bonds with two adjacent O_{2c} atoms. The most stable dissociation configuration is the formation of an O–H bond between a H atom of water and an adjacent O_{2c} atom (bridged OH_b), and of a bond between the remaining hydroxyl OH with the surface Ti_{5c} atom through the O atom (terminal hydroxyl OH_t). In previous reports [27, 53], it was also found that the most stable adsorption site of water on defect anatase TiO₂ (101) surface is the vacancy site at the OV, where the O atom of water molecule almost occupies the position of “bridged O_{2c} atom” in the vacancy, one hydrogen atom points to the adjacent bridged O_{2c} atom, and the other hydrogen atom points far away from the surface. In the corresponding dissociating adsorption state, the decomposed product oxygen atom becomes the bridged O_{2c} atom of surface, and bonds with one of the hydrogen atoms to form surface-terminated hydroxyl radical, while the other hydrogen atom is adsorbed onto adjacent bridged O_{2c} atom to form another surface-terminated hydroxyl radical. On the basis of existing research conclusions, a possible stable configuration of water adsorption on the surface is constructed and optimized, and the adsorption energy is obtained. The calculated adsorption configuration and adsorption energy are basically identical with previous studies [36, 53].

As shown in Fig. 10a, the most stable adsorption configuration for water on the surface of perfect anatase TiO₂ (101) is to combine with one Ti_{5c} atom and form weak hydrogen bonds with two adjacent O_{2c} atoms. In this state, the adsorption energy is 0.693 eV. The most stable dissociation configuration is that a hydrogen atom of water forms an –OH bond with adjacent O_{2c} atom, and the remaining hydroxyl (–OH) bonds with the surface Ti_{5c} atom through the oxygen atom. In this state, the adsorption energy is 0.400 eV. The process is endothermic. The adsorption energy of the transition state of the reaction is 0.026 eV. From the initial adsorbed molecular state, a H₂O molecule requires an overall activation energy of 0.719 eV to decompose, while the activation energy for its reverse reaction is 0.426 eV. So the dissociation is more difficult, and H₂O is more likely to undergo molecular adsorption. As shown in

Fig. 10b–d, a H₂O molecule is adsorbed at the same positions on the surfaces of anatase TiO₂ (101) with OV concentration of 1/8, 2/8 and 3/8 ML, separately. The most stable adsorption configuration is obtained by optimizing the adsorption model. The O atom of H₂O almost occupies the position of the bridged O_{2c} atom at the vacancy, one hydrogen atom points to adjacent bridged O_{2c} atom, and the other points away from the surface. By analyzing the transition states of water molecule dissociating on different surfaces, it is found that on the surface with OV concentration of 1/8 ML, H₂O molecule needs to absorb an energy of 1.183 eV to reach the transition state, while the reverse reaction activation energy is 1.837 eV. On the surface with OV concentration of 2/8 ML, H₂O molecule needs to absorb an energy of 1.315 eV to reach the transition state, while the reverse reaction activation energy is 1.692 eV. On the surface with OV concentration of 3/8 ML, H₂O molecule needs to absorb an energy of 1.545 eV to reach the transition state, while the reverse reaction activation energy is 2.057 eV. The overall water splitting reaction that occurs on the defect surface is exothermic, and the activation energy of the reverse reaction is much greater than that of the forward reaction, that is, the reaction more likely proceeds in the direction of dissociation. From the comparison of the water splitting reaction on the surface with OV concentration of 1/8 and 2/8 ML, the dissociation energy barrier of water molecule on the latter is increased by 0.132 eV, indicating that water splitting is more likely to occur on the former. On the other hand, the activation energy of the reverse reaction on the latter is 0.151 eV lower than that on the former, indicating that the water splitting products on the former are more stably adsorbed on the catalyst surface. When the OV concentration reaches 3/8 ML, the forward reaction barrier of water splitting reaction reaches 1.545 eV, and the reaction is more difficult to proceed. Figure 11 shows the dependence of the activation energy of the decomposition reaction (E_{act}) and the activation energy of the reverse reaction ($E_{\text{re-act}}$) on OV concentration. Consequently, the anatase (101) surface with OV concentration of 1/8 ML is more conducive to the water splitting reaction. From this point of view, the presence of OVs can indeed promote the progress of water splitting reaction, but as the concentration gets higher, its promotion effect weakens.

3.4 Photocatalytical hydrogen evolution performance

In order to verify the accuracy of computational results, the photocatalytical hydrogen production of anatase TiO₂ was experimentally conducted. In Fig. 12, the photocatalytical hydrogen production performance of TiO₂-NTAs treated at different temperatures is compared. Obviously, the hydrogen production performance of the black TiO₂ nanotube arrays obtained by the reduction of aluminum powder is significantly higher than that of control sample, indicating that OV can indeed improve the hydrogen production performance of the catalyst. There is a relatively large improvement in hydrogen production performance from 300°C to 450°C, but when the annealing temperature is further raised to 600°C, the improvement in hydrogen production performance is very weak. There is a flattening trend in the promotion of the photocatalytic reaction as OV concentration increases. These results prove that the calculation results are accurate.

4 Conclusion

In this work, the effect of oxygen vacancy concentration was investigated on the crystalline phase, electronic structure, and catalytic activity of TiO_2 through DFT calculations and experiments. The comparison between the measured XRD patterns of TiO_2 catalysts and the simulated XRD patterns of TiO_2 crystals validated the assumption that OV's cause change in the crystal structure and catalytic activity of TiO_2 . The changes in the electronic structure of anatase TiO_2 (101) as a function of OV concentration indicate that moderate OV concentration can improve the transition ability of electrons, but excessively high OV concentration may weaken this increase. In addition, the presence of oxygen vacancy does promote the progress of water splitting reaction, but as the concentration becomes higher, its promotion effect will be weakened. The modification of the electronic structure of anatase TiO_2 (101) with OV's is attributed mainly to the structure distortion and the electron transfer from OV's to Ti atoms, which leads to subsequent introduction of extra donor levels at the bottom of CB. Therefore, the electronic structure and catalytic performance of anatase TiO_2 can be effectively modulated by adjusting surface OV concentration.

Declarations

Acknowledgments

This work was supported by the Natural Science Foundation of China [62004137, 21878257; 21978196]; Natural Science Foundation of Shanxi Province [201701D221083]; Key Research and Development Program of Shanxi Province [201803D421079]; Scientific and Technological Innovation Programs of Higher Education Institutions in Shanxi [2019L0156]; Shanxi Provincial Key Innovative Research Team in Science and Technology [201605D131045-10]; and Research Project Supported by Shanxi Scholarship Council of China [2020-050].

Compliance with ethical standards

Conflict of interest No conflict of interest exists in the submission of this manuscript, and manuscript is approved by all authors for publication.

References

1. W.J. Ong, L.L. Tan, S.P. Chai, S.T. Yong, A.R. Mohamed, *ChemSusChem*. **7**, 690–719 (2014)
2. A. Fujishima, K. Honda, *Nature*. **238**, 37–38 (1972)
3. X. Chen, S. Shen, L. Guo, S.S. Mao, *Chem. Rev.* **110**, 6503–6570 (2010)
4. L. Yoong, F.K. Chong, B.K. Dutta, *Energy*. **34**, 1652–1661 (2009)
5. K. Hashimoto, H. Irie, A. Fujishima, *Jpn. J. Appl. Phys.* **44**, 8269–8285 (2005)
6. Q. Guo, C. Zhou, Z. Ma, X.M. Yang, *Adv. Mater.* **31**, 1901997 (2019)

7. X. Chen, S.S. Mao, Chem. Rev. **107**, 2891–2959 (2007)
8. B. Lahijani, K. Hedayati, M. Goodarzi, Main Group Met. Chem. **41**, 53–62 (2018)
9. Z. Ebrahimi, K. Hedayati, D. Ghanbari, J. Mater. Sci. Mater. Electron. **28**, 13956–13969 (2017)
10. K. Su, Z. Ai, L. Zhang, Phys. Chem. C **116**, 17118–17123 (2012)
11. Y.C. Zhang, N. Afzal, L. Pan, X.W. Zhang, J.J. Zou, Adv. Sci. **6**, 1900053 (2019)
12. G. Zhu, T. Lin, X. Lu, J. Mater. Chem. A **1**, 9650–9653 (2013)
13. I. Justicia, G. Garcia, L. Vazquez, J. Santiso, P. Ordejon, G. Battiston, R. Gerbasi, A. Figuerasa, Sensor Actuat. B-Chem. **109**, 52–56 (2005)
14. X.B. Chen, L. Liu, P.Y. Yu, S.S. Mao, Science **331**, 746–750 (2011)
15. F. Zuo, L. Wang, T. Wu, Z.Y. Zhang, D. Borchardt, P.Y. Feng, J. Am. Chem. Soc. **132**, 11856–11857 (2010)
16. J.Q. Gao, Q.Q. Shen, R.F. Guan, J.B. Xue, X.G. Liu, H.S. Jia, Q. Li, Y.C. Wu, J. CO₂ Util. **35**, 205–215 (2020)
17. T.L. Thompson, J.T. Yates, Top. Catal. **35**, 197–210 (2005)
18. Y. Hinuma, T. Toyao, T. Kamachi, Z. Maeno, S. Takakusagi, S. Furukawa, I. Takigawa, K. Shimizu, J. Phys. Chem. C **122**, 29435–29444 (2018)
19. M. Kong, Y. Li, X. Chen, T. Tian, P. Fang, F. Zheng, X.J. Zhao, Am. Chem. Soc. **133**, 16414–16417 (2011)
20. S.Q. Wei, F. Wang, M. Dan, K.Y. Zeng, Y. Zhou, Appl. Surf. Sci. **422**, 990–996 (2017)
21. H. Shi, Y.C. Liu, M. Miao, T. Wu, Q. Wang, Chem. Phys. Lett. **584**, 98–102 (2013)
22. D. Wang, H. Wang, P. Hu, Phys. Chem. Chem. Phys. **17**, 1549–1555 (2014)
23. D. Wang, T. Sheng, J.F. Chen, H.F. Wang, P. Hu, Nat. Catal. **1**, 291–299 (2018)
24. A. Barnard, P. Zapol, L. Curtiss, Surf. Sci. **582**, 173–188 (2005)
25. P. Maity, O.F. Mohammed, K. Katsiev, H. Idriss, J. Phys. Chem. C **122**, 8925–8932 (2018)
26. I.M. Nadeem, G.T. Harrison, A. Wilson, C.L. Pang, J. Phys. Chem. B **2**, 834–839 (2018)
27. J.P. Perdew, K. Burke, M. Ernzerhof, Phys. Rev. Lett. **77**, 1396–1396 (1997)
28. M.A. Ha, A.N. Alexandrova, J. Chem. Theory. Comput. **12**, 2889–2895 (2016)
29. J.Y. Liu, X.Q. Gong, A.N. Alexandrova, J. Phys. Chem. C **123**, 3505–3511 (2019)
30. C. Dette, M.A. Perez-Osorio, S. Mangel, F. Giustino, S.J. Jung, K. Kern, J. Phys. Chem. C **121**, 1182–1187 (2017)
31. W.Q. Chen, C. Tang, G. Zheng, Phys. B **404**, 1074–1078 (2009)
32. M. Arrigoni, G.K.H. Madsen, J. Chem. Phys. **152**, 044110 (2020)
33. G. Shukri, W.A. Dino, H.K. Dipojono, M.K. Augusta, H. Kasai, RSC Adv. **6**, 92241–92251 (2016)
34. U. Aschauer, Y. He, H. Cheng, S.C. Li, U. Diebold, A. Selloni, J. Phys. Chem. C **114**, 1278–1284 (2010)
35. W.J. Yin, B. Wen, Q.X. Ge, X.L. Wei, M.Y. Chen, L.M. Liu, Comp. Mater. Sci. **155**, 424–430 (2018)

36. Y. Cao, L. Ling, H. Lin, M.H. Fan, P. Liu, R.G. Zhang, B.J. Wang, *Comp. Mater. Sci.* **159**, 1–11 (2019)
37. U. Aschauer, Y. He, H. Cheng, S.C. Li, U. Diebold, A. Selloni, *J. Phys. Chem. C* **114**, 1278–1284 (2010)
38. R.G. Zhang, Z.X. Liu, L.X. Ling, B.J. Wang, *Appl. Surf. Sci.* **353**, 50–157 (2015)
39. M.T. Greiner, L. Chai, M.G. Helander, W.M. Tang, Z.H. Lu, *Adv. Funct. Mater.* **22**, 4557–4568 (2012)
40. S.T. Li, S.R. Shi, G.C. Huang, Y. Xiong, S.W. Liu, *Appl. Surf. Sci.* **455**, 1137–1149 (2018)
41. X. Li, S. Liu, K. Fan, Z.Q. Liu, B. Song, J.G. Yu, *Adv. Energy Mater.* **8**, 1800101 (2018)
42. Y. Wu, Y. Fu, L. Zhang, Y.H. Ren, X.Y. Chen, B. Yue, H.Y. He, *Chinese J. Chem.* **37**, 922–928 (2019)
43. M.H. Oza¹, D.K. Kanchan, J.H. Joshi, M.J. Joshi, *J. Mater. Sci. Mater. Electron.* **31**, 10177–10185 (2020)
44. Y.N. Hao, T.W. Chen, X. Zhang, H. Zhou, Y.C. Ma, *J. Chem. Phys.* **150**, 224702 (2019)
45. L. Kou, Th Frauenheim, A.L. Rosa, E.N. Lima, *J. Phys. Chem. C* **121**, 17417–17420 (2017)
46. Y. Nam, J.H. Lim, K.C. Ko, J.Y. Lee, *J. Mater. Chem. A* **7**, 13833–13859 (2019)
47. X. Pan, M.Q. Yang, X. Fu, N. Zhang, Y.J. Xu, *Nanoscale* **5**, 601–3614 (2013)
48. M. Elahifard, H. Heydari, R. Behjatmanesh-Ardakani, B. Peik, S. Ahmadvand, *J. Phys. Chem. Solids* **136**, 109176 (2019)
49. Z. Zhou, M. Li, L. Guo, *J. Phys. Chem. Solids* **71**, 1707–1712 (2010)
50. G.U. Oertzen, A.R. Gerson, *J. Phys. Chem. Solids* **68**, 324 – 330 (2007)
51. Y.B. He, A. Tilocca, O. Dulub, A. Selloni, U. Diebold, *Nat. Mater.* **8**, 585–589 (2009)
52. G. Fiscaro, S. Filice, S. Scalese, G. Compagnini, R. Reitano, L. Genovese, S. Goedecker, I. Deretzis, A. La Magna, *J. Phys. Chem. C* **124**, 2406–2419 (2020)
53. Z.Y. Zhao, Z.S. Li, Z.G. Zou, *J. Phys. Chem. C* **117**, 6172–6184 (2013)

Figures

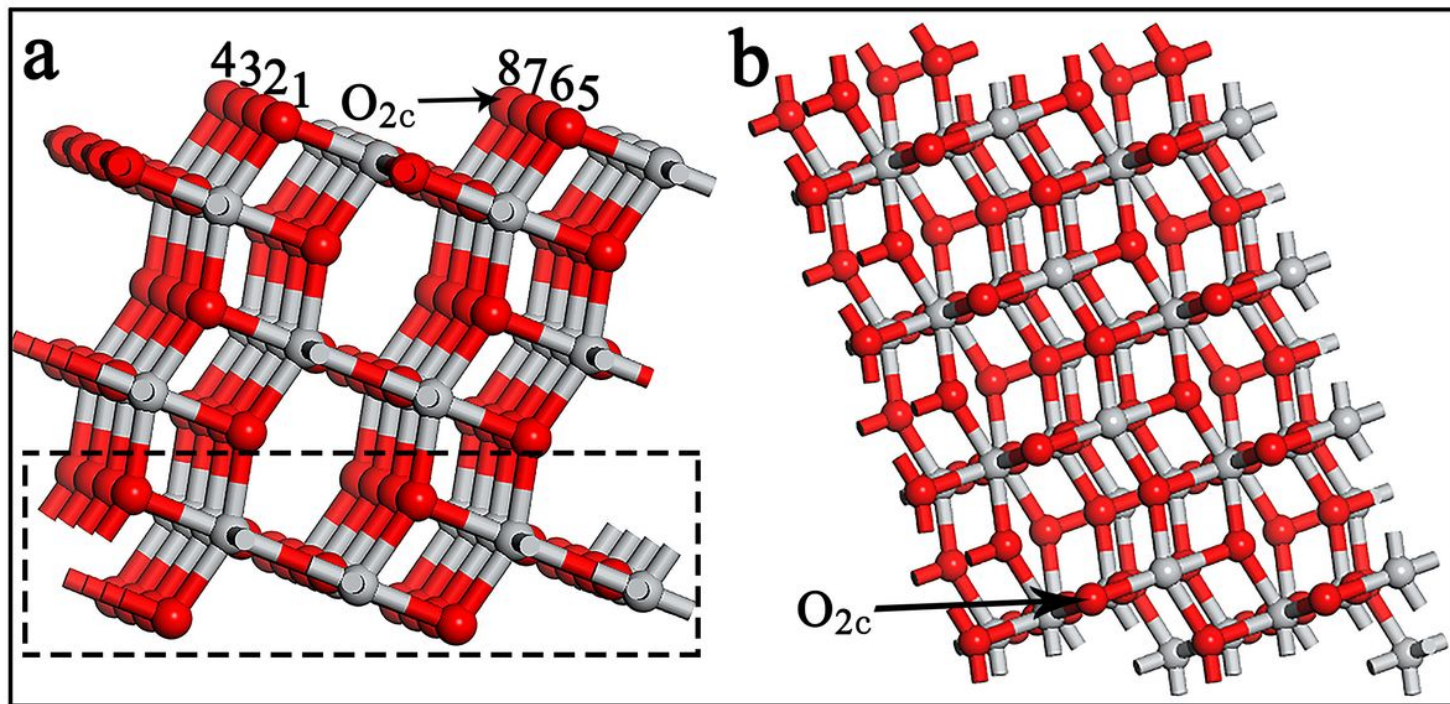


Figure 1

Side view (a) and top view (b) of perfect anatase TiO₂ (101) surface supercell constructed by (4 × 1) surface unit-cells

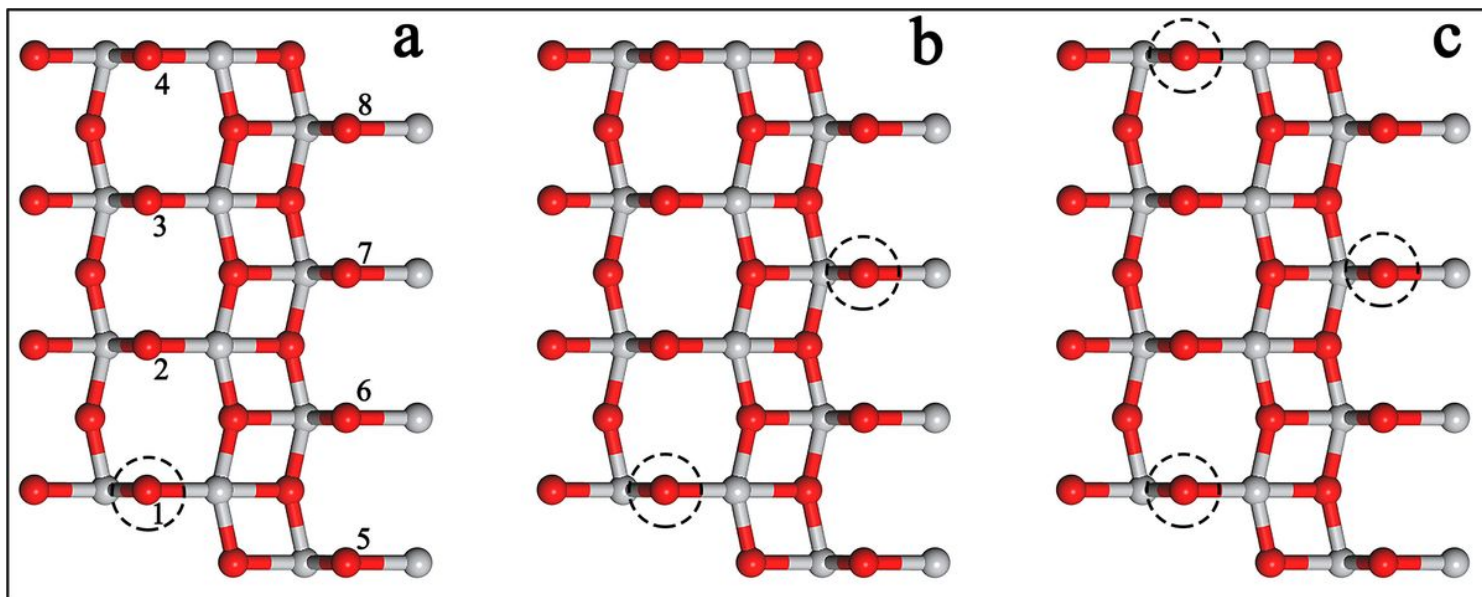


Figure 2

Top views of anatase TiO₂ (101) surfaces with 1/8 (a), 2/8 (b), and 3/8(c) ML OV, respectively

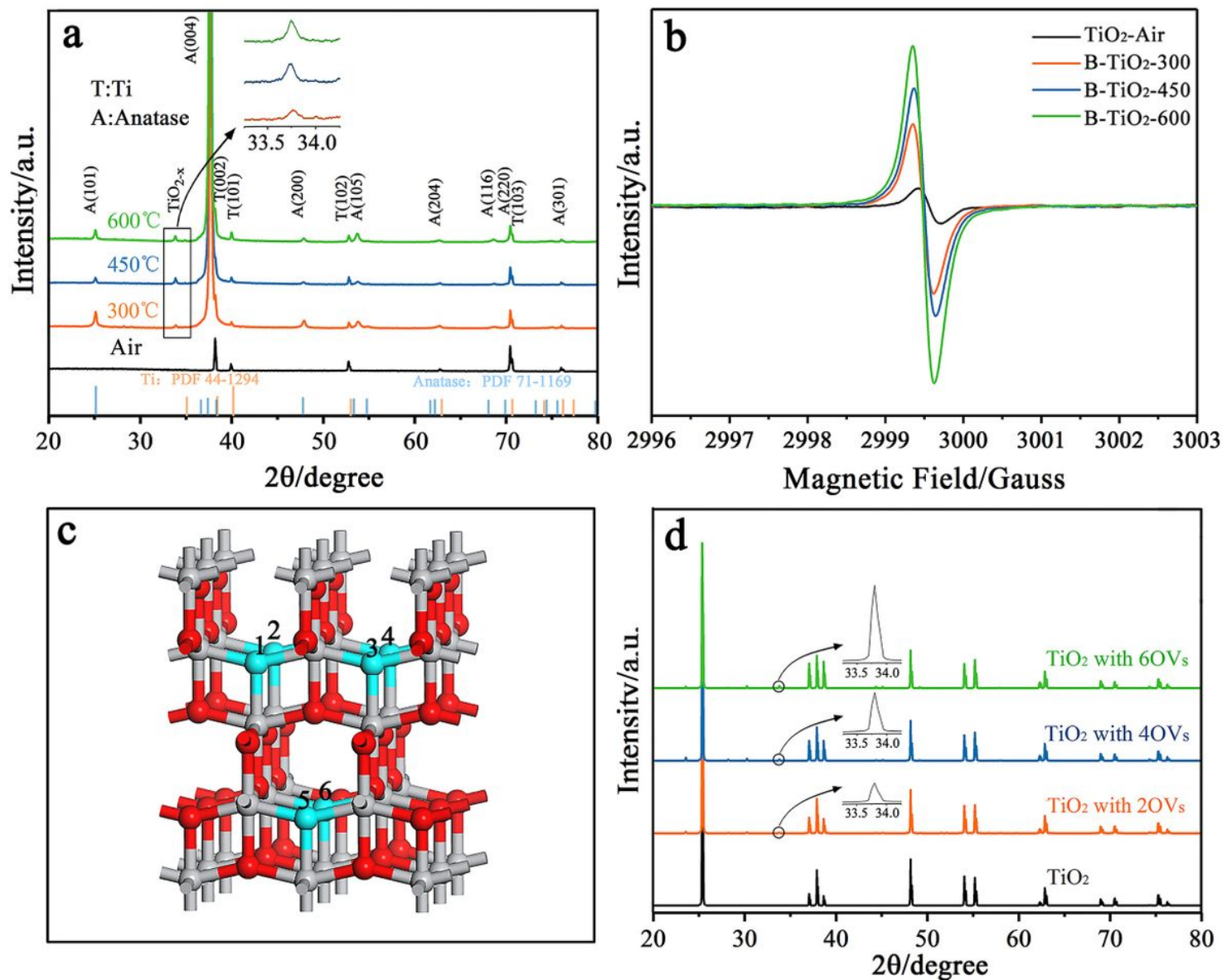


Figure 3

(a) Measured XRD patterns of TiO₂; (b) EPR spectra of black TiO₂ nanotube arrays; (c) TiO₂ (2 × 2 × 1) supercell model with a different number of OV; and (d) simulated XRD patterns of TiO₂ crystals with different numbers of OV

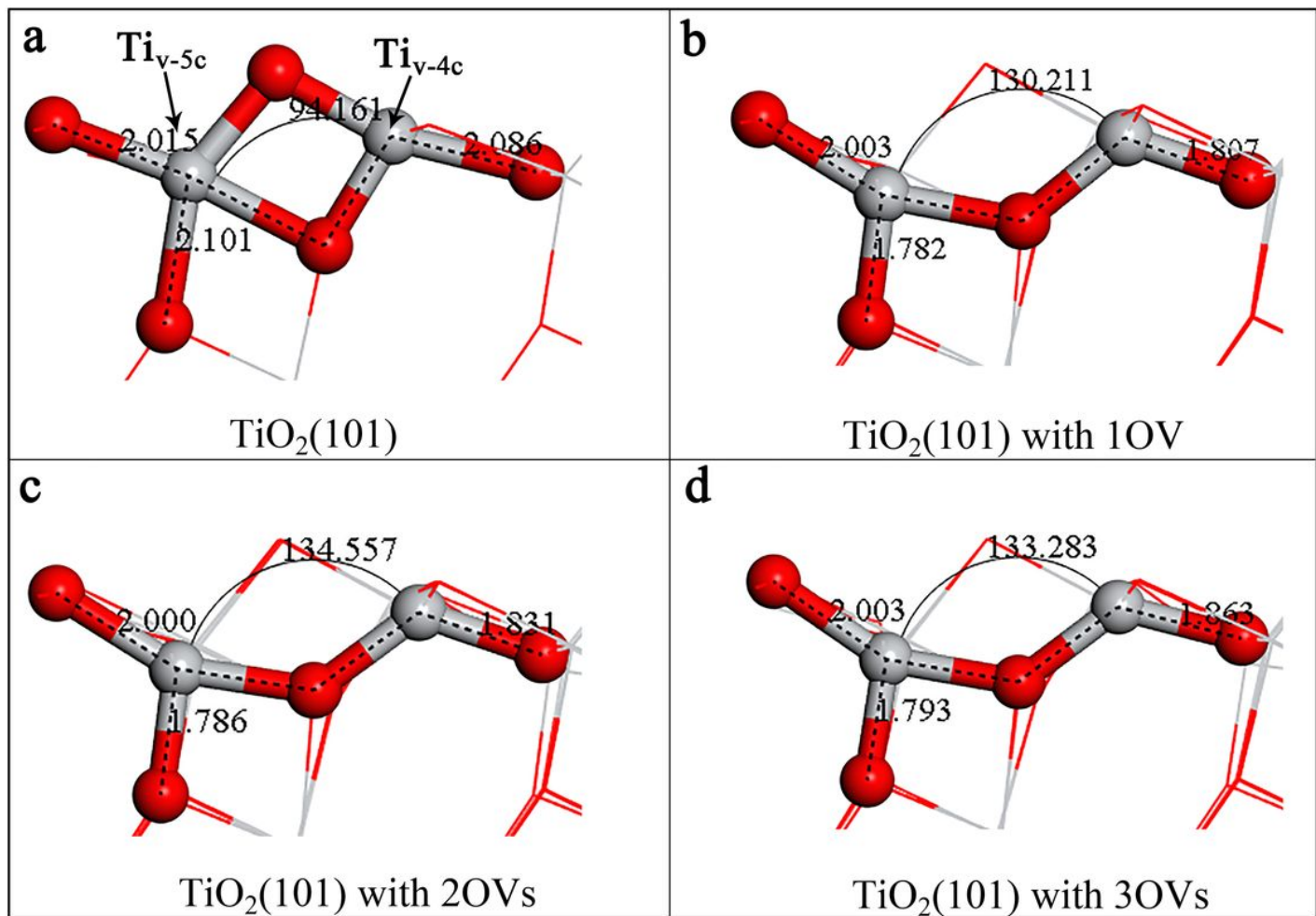


Figure 4

Local geometric structure of anatase TiO_2 (101) surfaces with 0 (a), 1/8 (b), 2/8 (c), and 3/8 (d) ML OVs, respectively

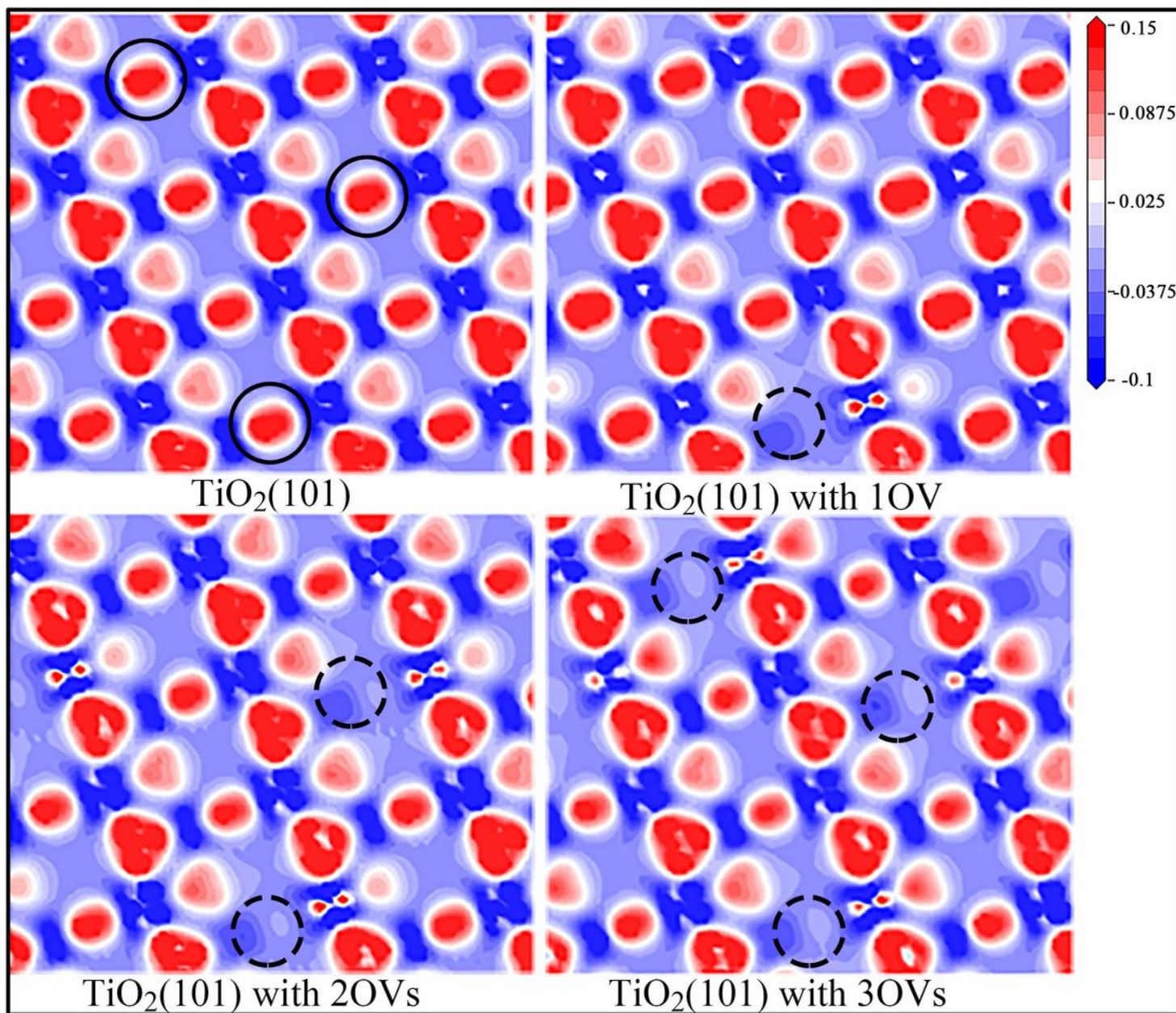


Figure 5

Density difference of anatase TiO₂ (101) surfaces with 0 (a), 1/8 (b), 2/8 (c), and 3/8 (d) ML OVs, respectively. Red areas represent electron enrichment and blue areas electron deficiency

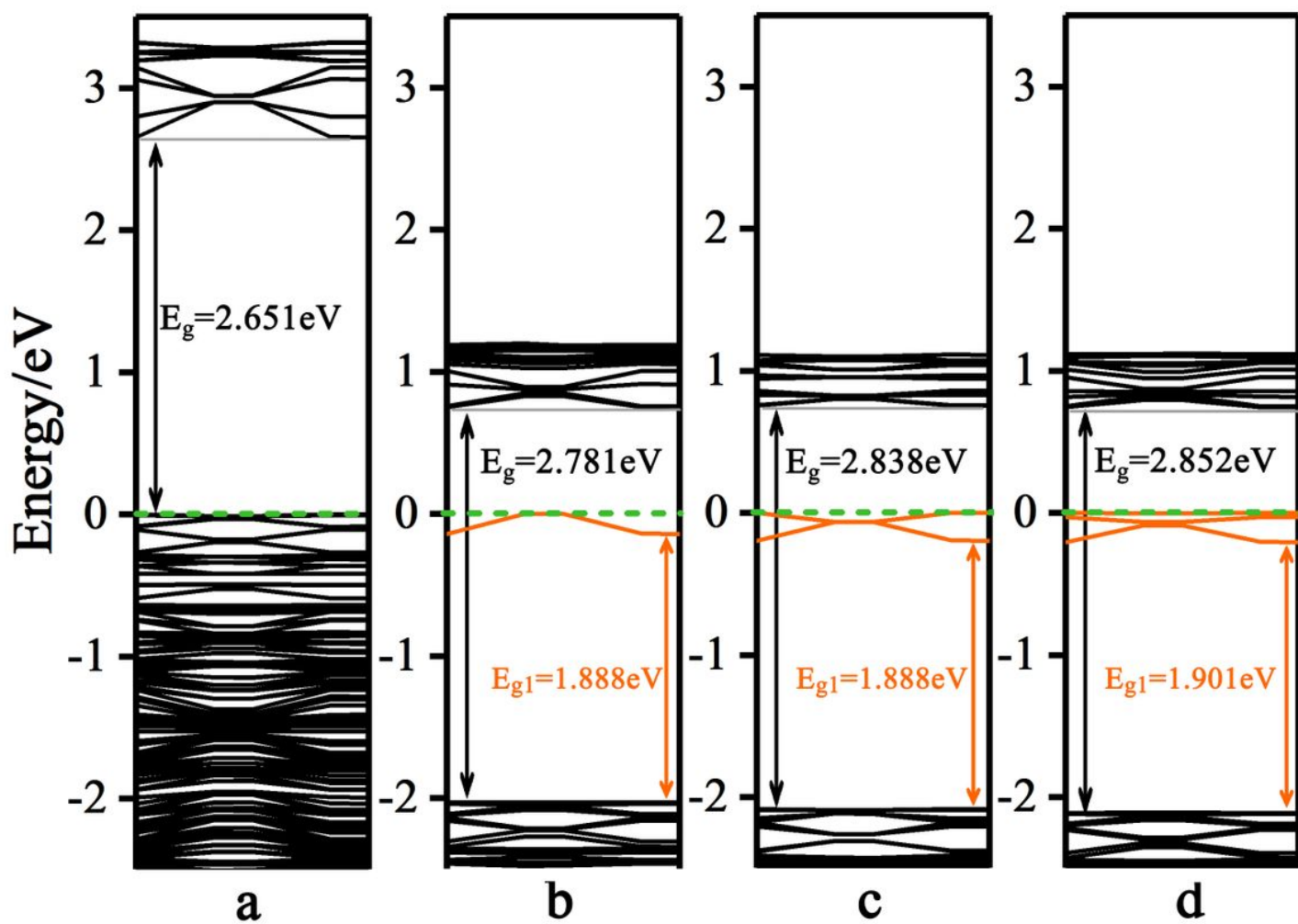


Figure 6

Band structures of anatase TiO₂ (101) surfaces with 0 (a), 1/8 (b), 2/8 (c), and 3/8 (d) ML OVs, respectively. The Fermi level and defect levels are highlighted in green and orange, respectively

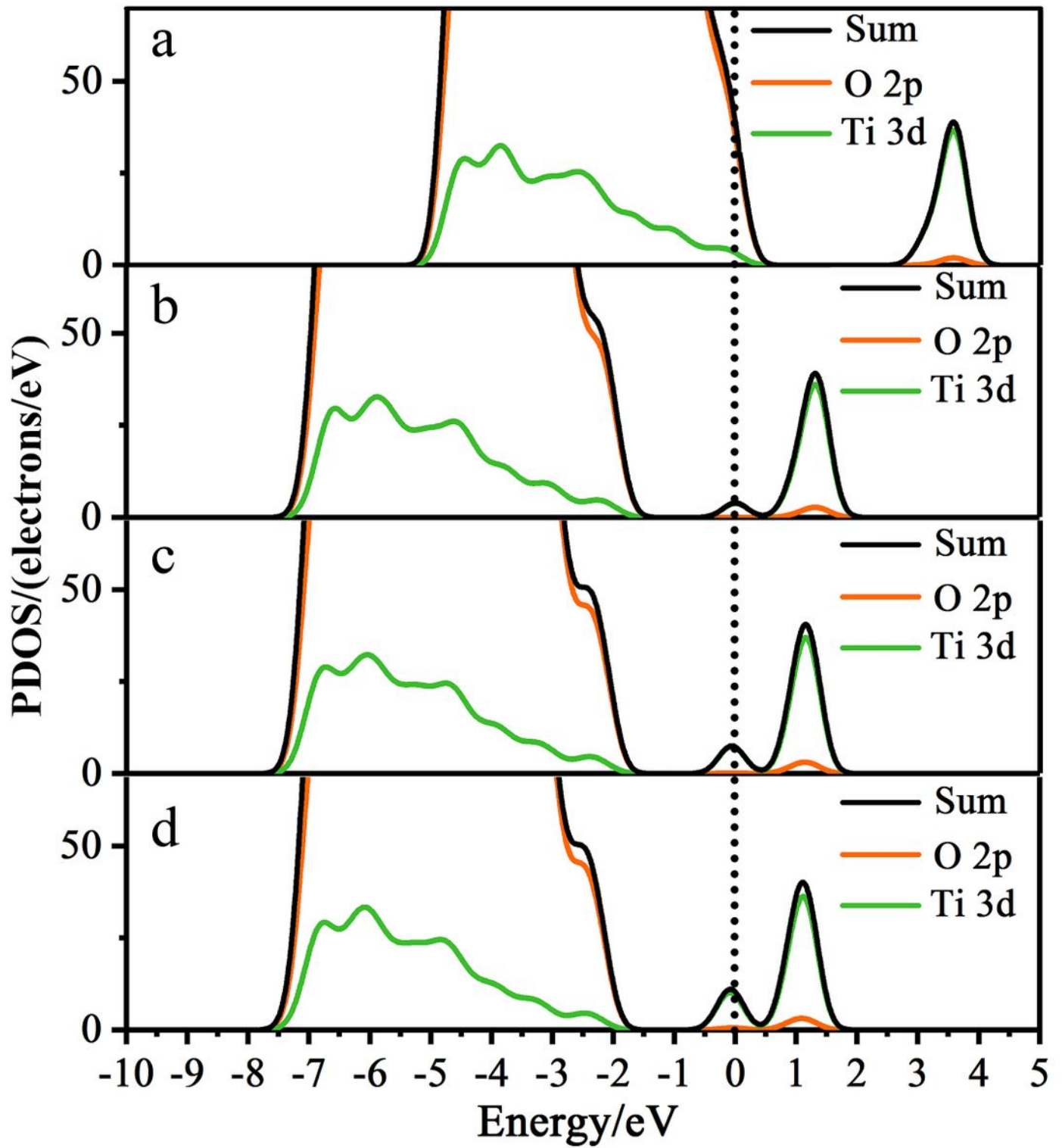


Figure 7

PDOS of anatase TiO₂ (101) surfaces with 0 (a), 1/8 (b), 2/8 (c), and 3/8 (d) ML OV_s, respectively

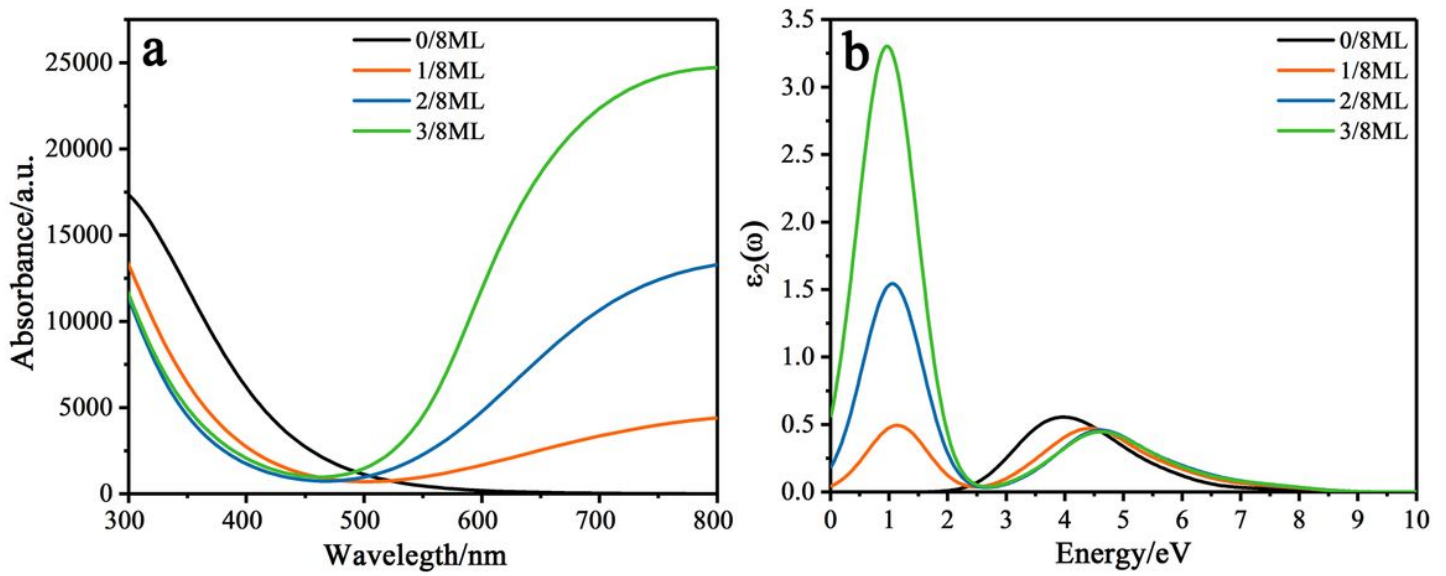


Figure 8

UV-vis absorption spectra (a) and dielectric function (b) of anatase TiO₂ (101) with different concentration of OVs

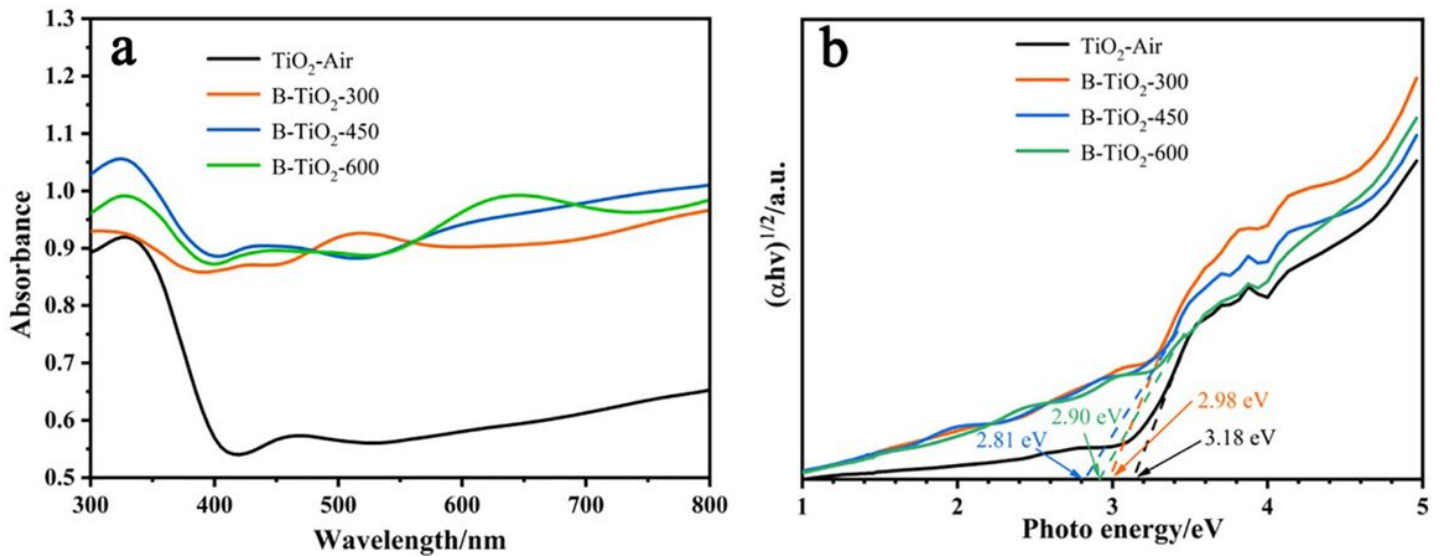


Figure 9

UV-vis diffuse reflectance absorption spectra (a) and determination of indirect interband transition energies (b)

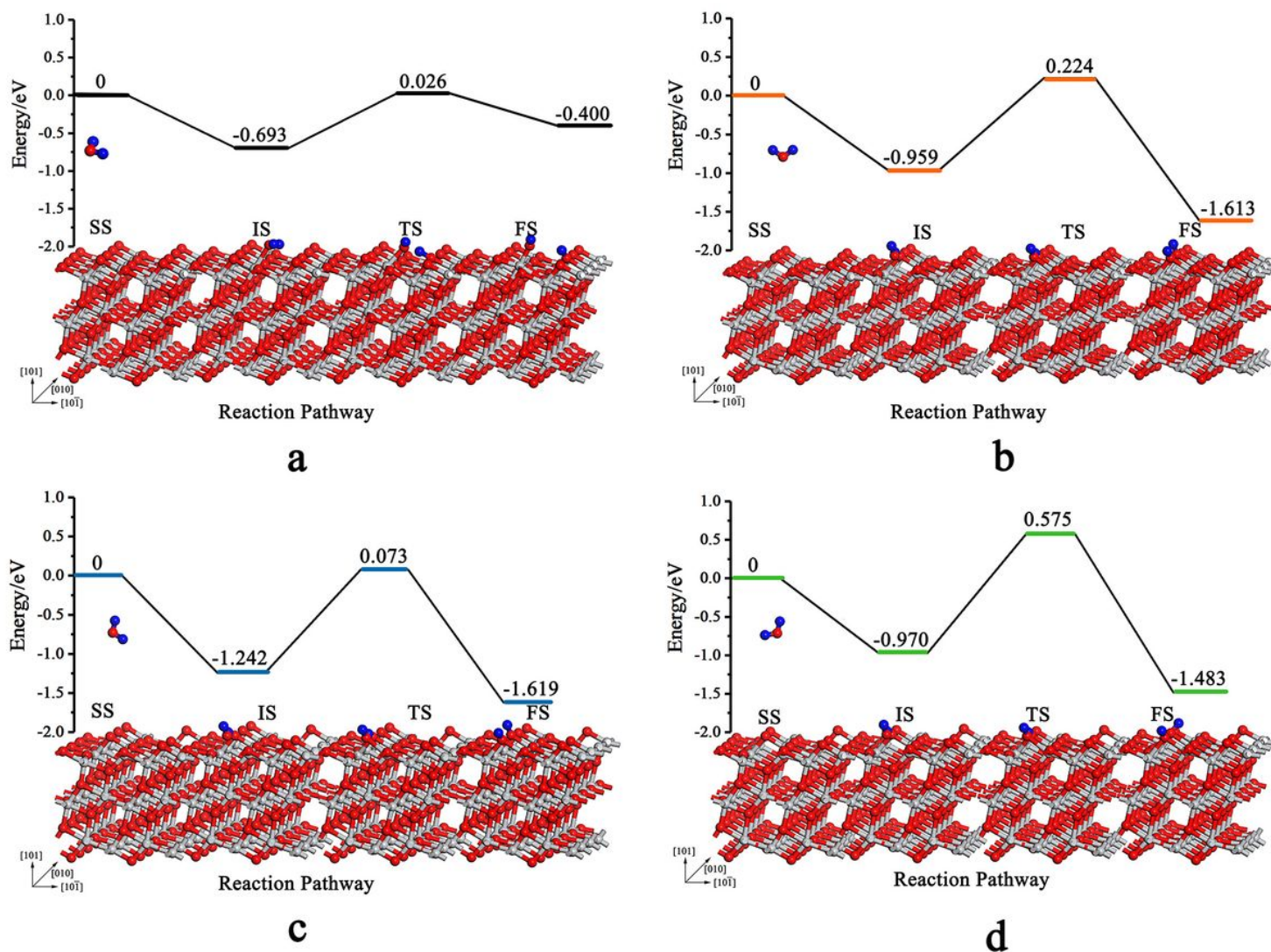


Figure 10

Adsorption configurations and decomposition reaction pathway of water on the anatase TiO₂ (101) surface with 0 (a), 1/8 (b), 2/8 (c), and 3/8 (d) ML OVs, respectively. "SS" denotes the separate state, "IS" the initial state, "TS" the transition state, and "FS" the final state

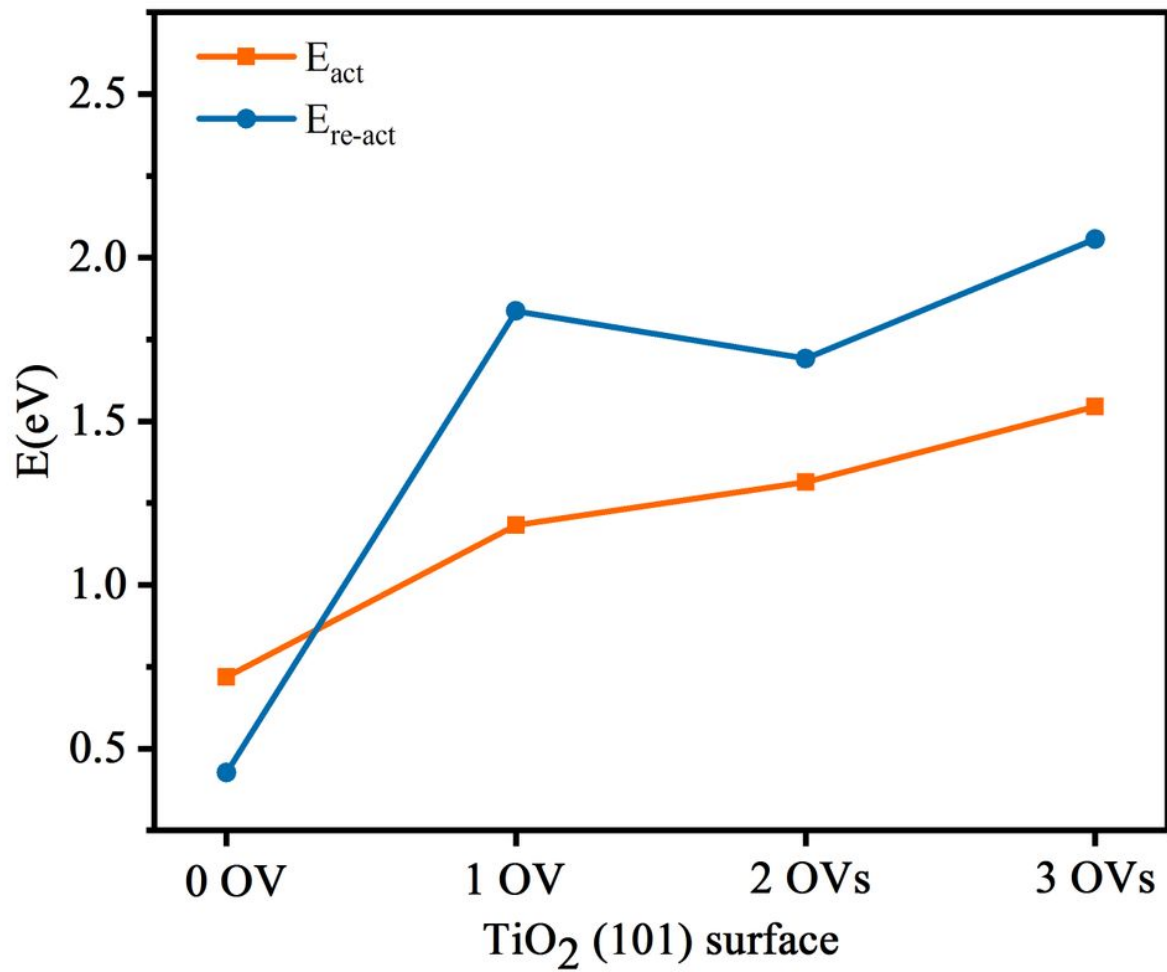


Figure 11

Change in the decomposition reaction activation energy (E_{act}) and the reverse reaction activation energy ($E_{\text{re-act}}$) as a function of OV concentration

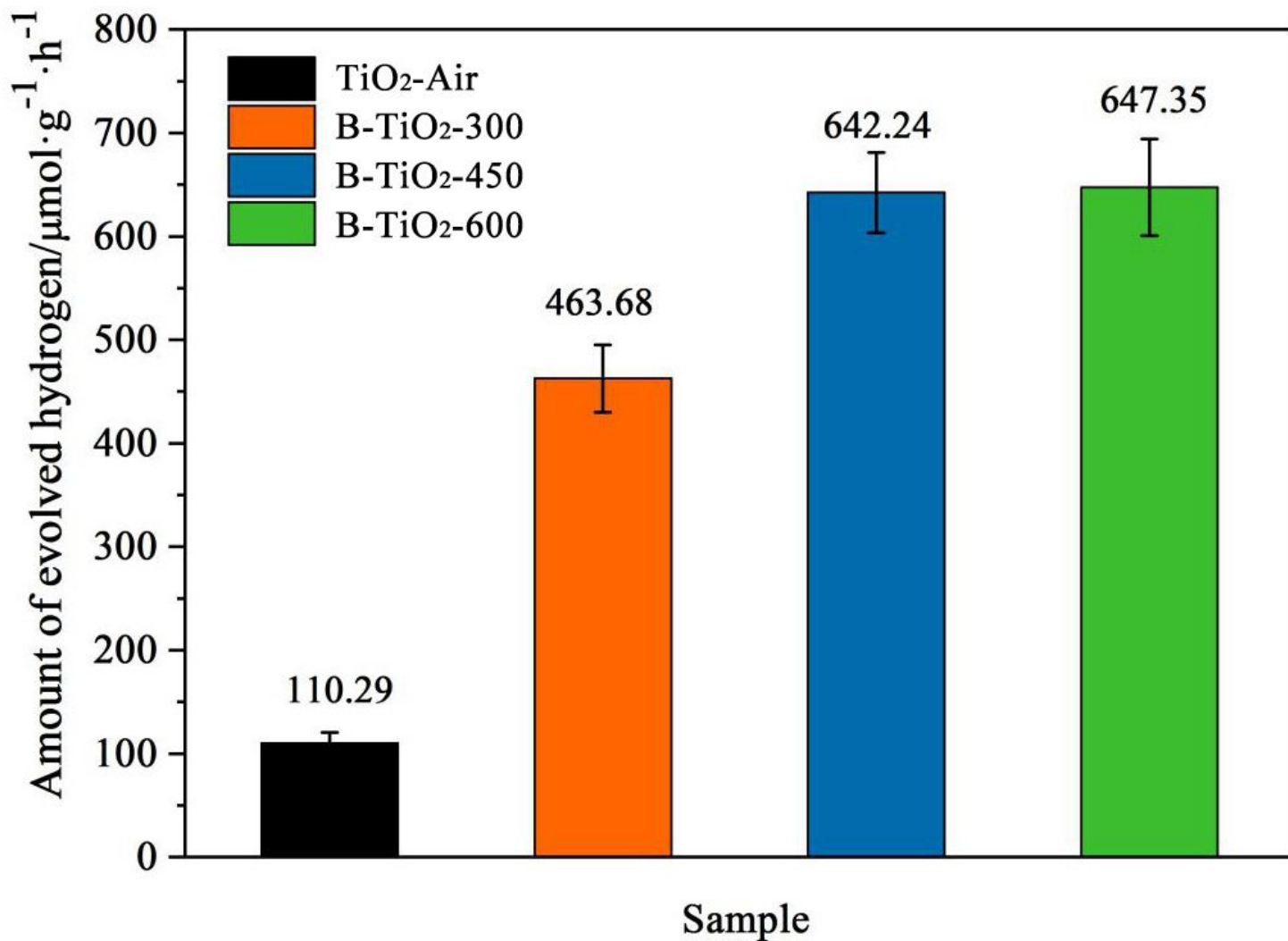


Figure 12

Comparison of photocatalytic hydrogen evolution rates